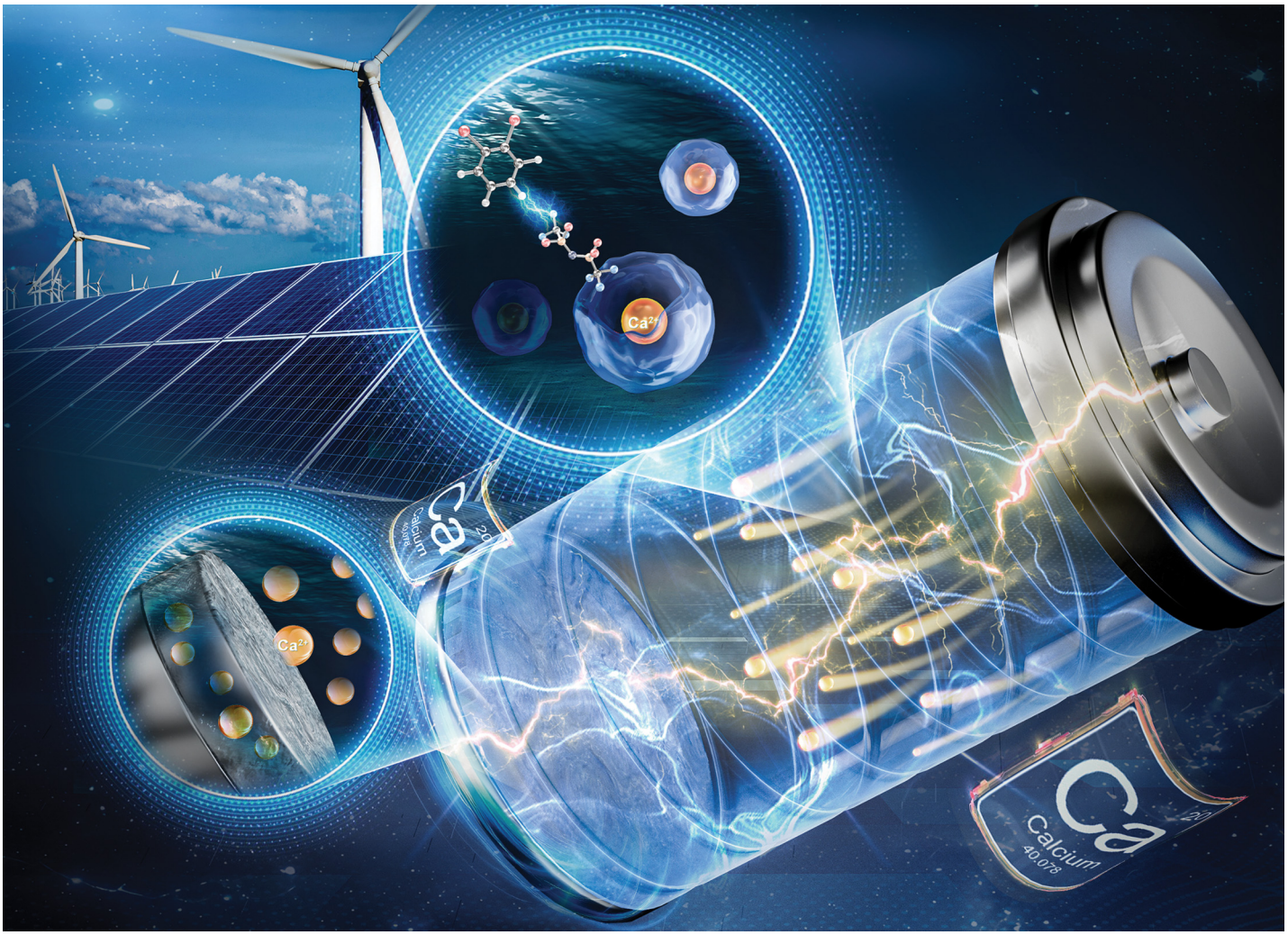

Showcasing research from Professor Zheng-Long Xu's laboratory, Department of Industrial and Systems Engineering, The Hong Kong Polytechnic University, Hong Kong SAR, China.

Anion-decoupled electrolytes enable stable cycling and fast interfacial kinetics for calcium metal anodes

Calcium metal batteries are promising candidates for next-generation energy storage, owing to their high energy density and the natural abundance of calcium. Nevertheless, reversible Ca metal cycling has long been hindered by anion-derived passivation layers in conventional electrolytes. In this work, we report an anion-decoupling strategy that promotes the formation of an organic-rich solid electrolyte interphase, enabling fast Ca^{2+} transport and stable plating/stripping at low overpotentials. Our findings establish a new electrolyte design paradigm for multivalent metal batteries, fundamentally distinct from the anion-coupling chemistry for Li metal anodes.

Image reproduced by permission of Zheng-Long Xu from *Energy Environ. Sci.*, 2026, **19**, 3203.

As featured in:

See Zheng-Long Xu *et al.*, *Energy Environ. Sci.*, 2026, **19**, 3203.

ROYAL SOCIETY OF CHEMISTRY

rsc.li/ees

Registered charity number: 207890

Energy & Environmental Science

ROYAL SOCIETY OF CHEMISTRY

PAPER

View Article Online
View Journal | View Issue

Cite this: *Energy Environ. Sci.*, 2026, **19**, 3203

Anion-decoupled electrolytes enable stable cycling and fast interfacial kinetics for calcium metal anodes

Qi Meng,[a] Zhen Zhan,[b] Yiyuan Ma,[a] Qi Qi,[a] Yingkai Hua,[a] Yuyang Yi,[a] Jingya Yu,[a] Mengcheng Wu,[a] Jingjing Tang,[e] Songhua Cai,[b] Kang Cheung Chan[ac] and Zheng-Long Xu *[acd]

Received 2nd December 2025,
Accepted 1st April 2026

DOI: 10.1039/d5ee07317k

rsc.li/ees

Calcium (Ca) metal batteries are a promising post-lithium-ion technology due to the high energy density of Ca and its crustal abundance. However, the strong cation–anion interactions of divalent Ca^{2+} in conventional electrolytes promote the formation of a Ca^{2+} ion-blocking solid electrolyte interphase (SEI) that hinders Ca metal electrodeposition. Here, we introduce an anion-decoupling strategy that combines a strongly coordinating solvent, dimethylacetamide (DMAc), with an anion-pulling 1,2-dibromobenzene (1,2-DBB) additive to regulate the widely accessible $Ca(TFSI)_2$-based electrolytes for reversible Ca metal anodes. Spectroscopic and theoretical analyses reveal that DMAc induces a solvent-rich coordination structure and suppresses Ca^{2+}-$TFSI^-$ ion pairs, while 1,2-DBB further pulls $TFSI^-$ out of the primary solvation shell, hindering its decomposition into unfavorable CaF_2 in the SEI. The resulting inorganic-poor SEI enables fast Ca^{2+} transport and highly reversible Ca metal plating/stripping at low overpotentials of <0.19 V, compared to those of >5 V in conventional $Ca(TFSI)_2$ electrolytes. The optimized electrolyte supports stable cycling of Ca//Ca symmetric cells for over 340 hours and delivers $>90\%$ capacity retention over 200 cycles in Ca//graphite and Ca//9,10-phenanthrenequinone full cells. This work establishes anion-decoupling electrolyte chemistry, distinct from the well-established anion-coupling electrolyte chemistry for monovalent metal anodes (Li and Na), enabling fast interfacial kinetics and stable cycling of divalent metal anodes.

Broader context

With performance requirements constantly increasing for energy storage devices, there is much demand for highly affordable and high-energy density batteries that extend the capabilities of conventional lithium-ion systems. For battery anodes, calcium (Ca) metal is considered to be one of the most attractive choices because of its negative electrochemical potential, exceptional nature abundance, and high theoretical capacities. However, reversible cycling of Ca metal in aprotic organic electrolytes has been extremely difficult due to the anion-derived Ca ion-blocking passivation layers. Unlike monovalent Li electrolytes, divalent Ca electrolytes exhibit stronger cation–anion coordination that promotes anion decomposition and the aggressive formation of inorganic-rich solid–electrolyte interphases (SEIs). To address these fundamental challenges, this work introduces a two-pronged approach that decouples Ca ion–anion pairs in the bulk electrolyte and stabilizes the anion species to promote the formation of organic-rich SEI layers. The tailored interface supports fast Ca ion transport and enables Ca metal stripping/plating with low overpotentials. The anion-decoupling electrolyte design diverges conceptually from the widely explored anion-coupling paradigm for Li metal anodes, which offers a new mechanistic framework for advancing multivalent metal battery chemistries.

[a] *Department of Industrial and Systems Engineering, The Hong Kong Polytechnic University, Hung Hom, Hong Kong SAR, China. E-mail: zhenglong.xu@polyu.edu.hk*
[b] *Department of Applied Physics, The Hong Kong Polytechnic University, Hung Hom, Hong Kong, China*
[c] *Research Institute for Advanced Manufacturing, The Hong Kong Polytechnic University, Hung Hom, Hong Kong SAR, China*
[d] *Shenzhen Research Institute, The Hong Kong Polytechnic University, Shenzhen, China*
[e] *School of Metallurgy and Environment, Central South University, Changsha, China*

1. Introduction

Driven by the rapid expansion of the electrochemical energy storage market, post-lithium metal batteries have emerged as promising alternatives to current Li-ion batteries, owing to their potential for higher energy densities from metal anodes and better affordability from abundant elements.[1–3] Among the post-Li battery systems, calcium (Ca) metal batteries are particularly promising due to their low electrochemical potential (−2.87 V *vs.* the standard hydrogen electrode), high theoretical

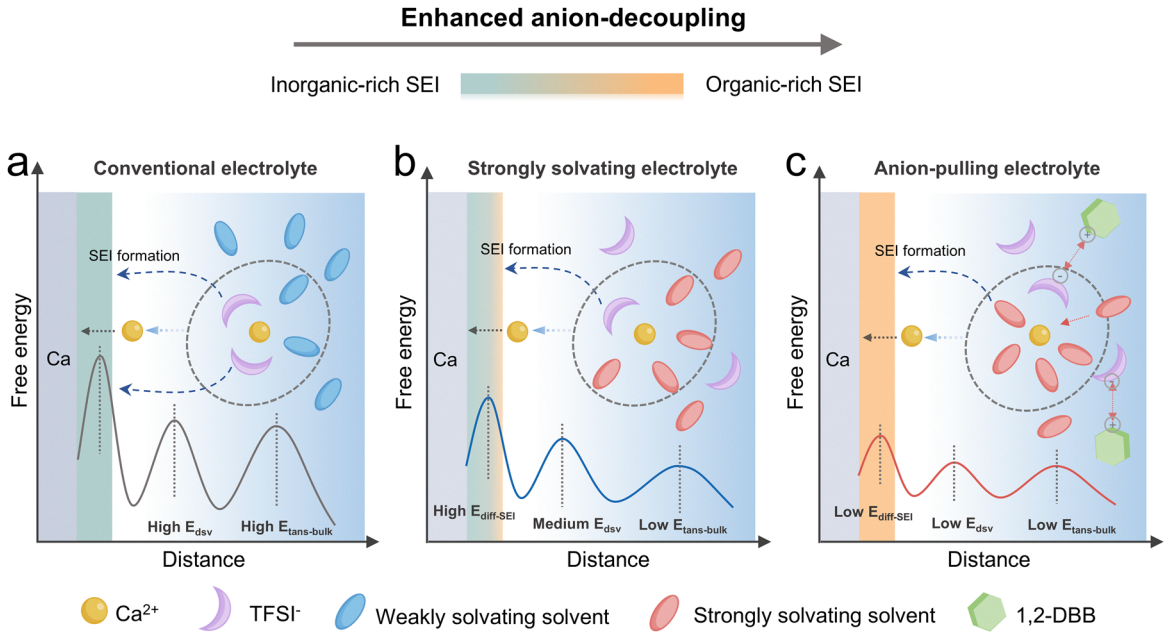

Fig. 1 Schematic illustration of the anion-decoupling mechanism. The Ca^{2+} migration and reduction processes in (a) conventional electrolyte, (b) strongly solvating electrolyte and (c) anion-pulling electrolyte. $E_{trans\text{-}bulk}$, E_{dsv} and $E_{diff\text{-}SEI}$ represent the energy barriers for Ca^{2+} transport in the bulk electrolyte, desolvation at the interface, and diffusion through the SEI, respectively.

capacities (1337 mAh g^{-1} and 2073 mAh cm^{-3}), excellent thermal stability (melting point: ~842 °C), and crustal abundance (ranking as the 5th richest element in the Earth's crust).[4–7] Nevertheless, reversible Ca metal anodes with compelling stripping/plating reaction kinetics remain inaccessible in most organic electrolytes.

The problem roots in two intrinsic constraints. First, compared to monovalent cations like Li^+ and Na^+, Ca^{2+} with stronger electrostatic interactions hinders the ion-pair dissociation, leading to sluggish ion transport in the bulk electrolyte and high energy barriers for ion desolvation at the anode/electrolyte interface.[8–10] Second, the aggressive decomposition of anions in organic electrolytes readily forms thick and ionically insulating inorganic phases on the surface of the Ca metal, thus disabling reversible Ca plating/stripping reactions (Fig. 1a).[11–14] Given the critical role of the electrolyte in determining the solid electrolyte interphase (SEI) chemistry and interfacial kinetics,[15–17] rational electrolyte design is under the spotlight for advancing Ca metal batteries. The first reversible Ca metal anode was achieved using a $Ca(BF_4)_2$–ethylene carbonate (EC)/propylene carbonate (PC) electrolyte.[18] The strong Ca^{2+}–BF_4^- ion pair coupling and the CaF_2-rich SEI layers demanded elevated temperatures of above 75 °C to activate effective Ca ion migration.[10] Room-temperature operation of Ca metal anodes was realized in a $Ca(BH_4)_2$/tetrahydrofuran (THF) electrolyte.[19] The relatively conductive CaH_2 component in the SEI from BH_4^- decomposition was found to enable Ca metal cycling at moderate overpotentials (<0.5 V). However, the narrow electrochemical stability window (<2.5 V) and the high cost of borohydride salts limit their practicality for Ca metal batteries using high-voltage cathodes. To weaken Ca^{2+}–anion coordination, large and weakly coordinating anions such as $[B(hfip)_4]^-$,[20,21] $(CB_{11}H_{12})^-$,[22] and $[Al(hfip)_4]^-$ (ref. 23) have been developed for reversible Ca metal anodes, but their practicality is limited by the expensive precursors and complex syntheses.

By contrast, $Ca(TFSI)_2$ is an affordable and widely available salt, but the strong Ca^{2+}–$TFSI^-$ interactions in organic electrolytes have demonstrated irreversibility for Ca metal anodes. This behavior contrasts with monovalent-ion (*i.e.*, Li^+ and Na^+) electrolyte systems, which prefer weakly solvating solvents (*e.g.*, fluorinated ethers) and enhanced contact-ion-pair (CIP) or aggregate (AGG) solvation structures to yield inorganic-rich SEI layers (*i.e.*, LiF and NaF),[24–26] thus stabilizing metal surfaces and promoting the uniform deposition of Li and Na metal anodes.[27,28] In contrast, in the $Ca(TFSI)_2$–DME or EC/PC electrolytes, the tightly bound Ca^{2+}–$TFSI^-$ complexes lead to the formation of passivation layers mainly containing CaF_2, CaO and $CaCO_3$,[29,30] which impose pronounced Ca^{2+} migration energy barriers (>1 eV).[1,10,31] To alleviate the formation of inorganic-rich SEIs, strongly coordinating co-solvents (*i.e.*, 4-methoxybutan-2-amine added in $Ca[B(hfip)_4]_2$–DME (G1) electrolyte)[32] and ionic liquids (*i.e.*, $EmimBF_4$ added in $Ca(TFSI)_2$–dimethyl sulfoxide (DMSO) electrolyte)[33] have been introduced to decrease the coordination between anions and Ca^{2+}. Although the cycling lifespan of Ca metal anodes was extended, the overpotential remains above 0.5 V. Therefore, developing new electrolytes or strategies that can unlock $Ca(TFSI)_2$-based electrolytes enabling reversible Ca plating/stripping with low overpotentials remains challenging.

In this work, we introduce a two-pronged approach by systematically screening strongly coordinating solvents to reinforce Ca^{2+}–solvent coordination (Fig. 1b) and an anion-pulling

additive, 1,2-dibromobenzene (1,2-DBB), to further extract $TFSI^-$ out of the primary solvation shell in $Ca(TFSI)_2$-based electrolytes (Fig. 1c). Theoretical calculations of solvation strengths across a series of solvents (*i.e.*, ethers, carbonates, amides, and sulfoxides) in $Ca(TFSI)_2$-based electrolyte solutions, correlated with the electrochemical responses of Ca metal anodes, reveal a direct relationship between Ca reversibility and the ion-pair decoupling capability, thus identifying dimethylacetamide (DMAc) as the optimal solvent in this system. Although DMAc solvent has been explored for Ca anodes, strong cation–anion coupling persists and interfacial kinetics remain sluggish,[34] necessitating the introduction of ''anion-pulling'' chemistry to overcome this performance hurdle. By comparing the binding energies of halogen–benzene molecules with $TFSI^-$, 1,2-dibromobenzene (1,2-DBB) is selected as an effective additive for weakening Ca^{2+}–$TFSI^-$ coordination. Spectroscopic and theoretical analyses demonstrate that the 1,2-DBB additive modulates the solvation structure and increases the chemical bond orders of $TFSI^-$ anions, thereby suppressing the decomposition of $TFSI^-$ into unfavorable inorganic compounds in the SEI as demonstrated by high-resolution transmission electron microscopy (HRTEM) observations. The resulting $Ca(TFSI)_2$–DMAc/1,2-DBB electrolyte exhibits high ionic conductivity (σ = 12.75 mS cm^{-1}), low desolvation energy barriers (ΔE = 27.02 kJ mol^{-1}), and accelerated Ca^{2+} transport kinetics through the electrode/electrolyte interface. Consequently, Ca//Ca symmetric cells operate with low overpotentials ($<$0.2 V *vs.* $>$ 5 V in conventional $Ca(TFSI)_2$-G1, EC/PC, or THF electrolytes) and extended cycle life (over 340 hours). The superiority of our anion-decoupled electrolytes is also demonstrated by the excellent cyclability of Ca//graphite (over 200 cycles with $>$90% capacity retention) and Ca//9,10-phenanthrenequinone (PQ) full cells (290 cycles at 50 mA g^{-1}). Overall, this work unlocks the feasibility of $Ca(TFSI)_2$-based electrolytes that were previously unsuitable for Ca metal anodes through anion-decoupling chemistry. Our findings emphasize fundamentally different electrolyte design principles from those established in monovalent metal anode systems, offering new insights towards developing feasible electrolytes for multivalent metal batteries.

2. Results and discussion

2.1 Strongly coordinating solvents for decoupling Ca^{2+}–$TFSI^-$ pairs

Density functional theory (DFT) calculations of the binding energy differences (ΔE) between the representative alkali and alkaline earth metal ions (*e.g.*, Li^+, Na^+, K^+, Ca^{2+}, and Mg^{2+}) with typical solvents (*e.g.*, G1, THF, and EC) and $TFSI^-$ anions reveal that ΔE for divalent ions (Ca^{2+} and Mg^{2+}) are two times higher than those of monovalent ions (Li^+, Na^+, and K^+) across all the representative solvents (Fig. 2a). This result illustrates the stronger cation–anion coupling strength in Ca-based electrolyte systems. Notably, Ca^{2+} presents stronger binding energies with $TFSI^-$ than FSI^-, OTF^-, and BF_4^- (Fig. S1), highlighting the difficulty in decoupling Ca^{2+}–$TFSI^-$ ion pairs in the electrolyte. Furthermore, the lowest unoccupied molecular orbital (LUMO) energy levels of $TFSI^-$ shift markedly from 0.12 eV (free anion) to −0.68 eV upon coupling with Ca^{2+} (Fig. S2a). The strong Ca^{2+}–$TFSI^-$ interaction reduces the Mayer bond orders across the internal bonds (C–F, S–N, and S–O) in $TFSI^-$, thus enhancing their cleavage tendency to form the CaF_2-rich SEI (Fig. S2b).[35] It was reported that CaF_2 exhibits the largest Ca^{2+} migration energy barriers ($\sim$2046 meV) among the potential inorganic SEI components (*i.e.*, $\sim$997 meV for CaO, $\sim$540 meV for CaH_2, and $\sim$1436 meV for $CaCO_3$).[10] Therefore, it is essential to exclude $TFSI^-$ from the primary solvation shell and suppress its decomposition for feasible Ca metal cycling in the $Ca(TFSI)_2$-based electrolytes.

To approach a solvent-rich and anion-poor solvation configuration, we examined the donor number (DN) and the minimum electrostatic potential (ESP_{min}) of ten representative solvent molecules, including ethers, carbonates, amides, and sulfoxide. The DN reflects the tendency of electron donating ability of a solvent towards cations,[36] while ESP_{min} represents the lowest electrostatic potential on the solvent surface, indicating the strength of cation–solvent interactions.[37] Accordingly, solvents with high DN and large $|ESP_{min}|$ are expected to deliver strong coordination with Ca^{2+}. Fig. S3 and Fig. 2b summarize the $|ESP_{min}|$ and DN distributions of nine representative solvents, which shows that amides (dimethylformamide (DMF) and DMAc) and the sulfoxide (DMSO) lie in the upper-right region with a DN of $>$26 kcal mol^{-1} and an $|ESP_{min}|$ of $>$44 kcal mol^{-1}, identifying them as highly coordinating solvent candidates. Ethers (*i.e.*, dioxolane DOL, G1, diglyme G2, and tetraglyme G4) and carbonates (*i.e.*, EC and PC) present relatively low DN ($<$15 kcal mol^{-1}) or $|ESP_{min}|$ ($<$30 kcal mol^{-1}).

To validate this prediction, Raman measurements and molecular dynamics (MD) simulations were performed for 0.3 M $Ca(TFSI)_2$ G1 (a weakly coordinating solvent) and 0.3 M $Ca(TFSI)_2$ DMAc (a strongly coordinating solvent) electrolyte solutions. Raman spectra related to the S–N–S vibration of $TFSI^-$ reveal that the coordinated $TFSI^-$ species (at 749.5 cm^{-1}) predominate in the G1-based electrolyte, whereas the free $TFSI^-$ peak (at 738.9 cm^{-1}) is more pronounced in the DMAc-based electrolyte (Fig. S4). MD simulations further reveal the distinct solvation features: the $Ca(TFSI)_2$-G1 electrolyte exhibits pronounced aggregations of Ca^{2+}–$TFSI^-$ ion pairs (Fig. S5a), whereas $Ca(TFSI)_2$–DMAc displays more dispersed solvated ion pair configurations (Fig. S5b). Radial distribution functions (RDFs) show a higher coordination number of 3.5 for $Ca–O_{TFSI^-}$ (oxygen in $TFSI^-$) in the $Ca(TFSI)_2$–G1 electrolyte than that of 2.1 for the $Ca(TFSI)_2$–DMAc electrolyte (Fig. S5c), indicating more Ca^{2+}–$TFSI^-$ ion pairs in the former electrolyte. On the other hand, the coordination number for the solvent ($Ca–O_{solvent}$) increases from 4.6 in the G1-based electrolyte to 5.7 in the DMAc-based electrolyte (Fig. S5d). These comparisons corroborate the effectiveness of DMAc solvent with high DN and $|ESP_{min}|$ values in decoupling $TFSI^-$ from Ca^{2+}.

The improved ion decoupling translates directly to enhanced ion transport in the bulk electrolyte. Strongly coordinating

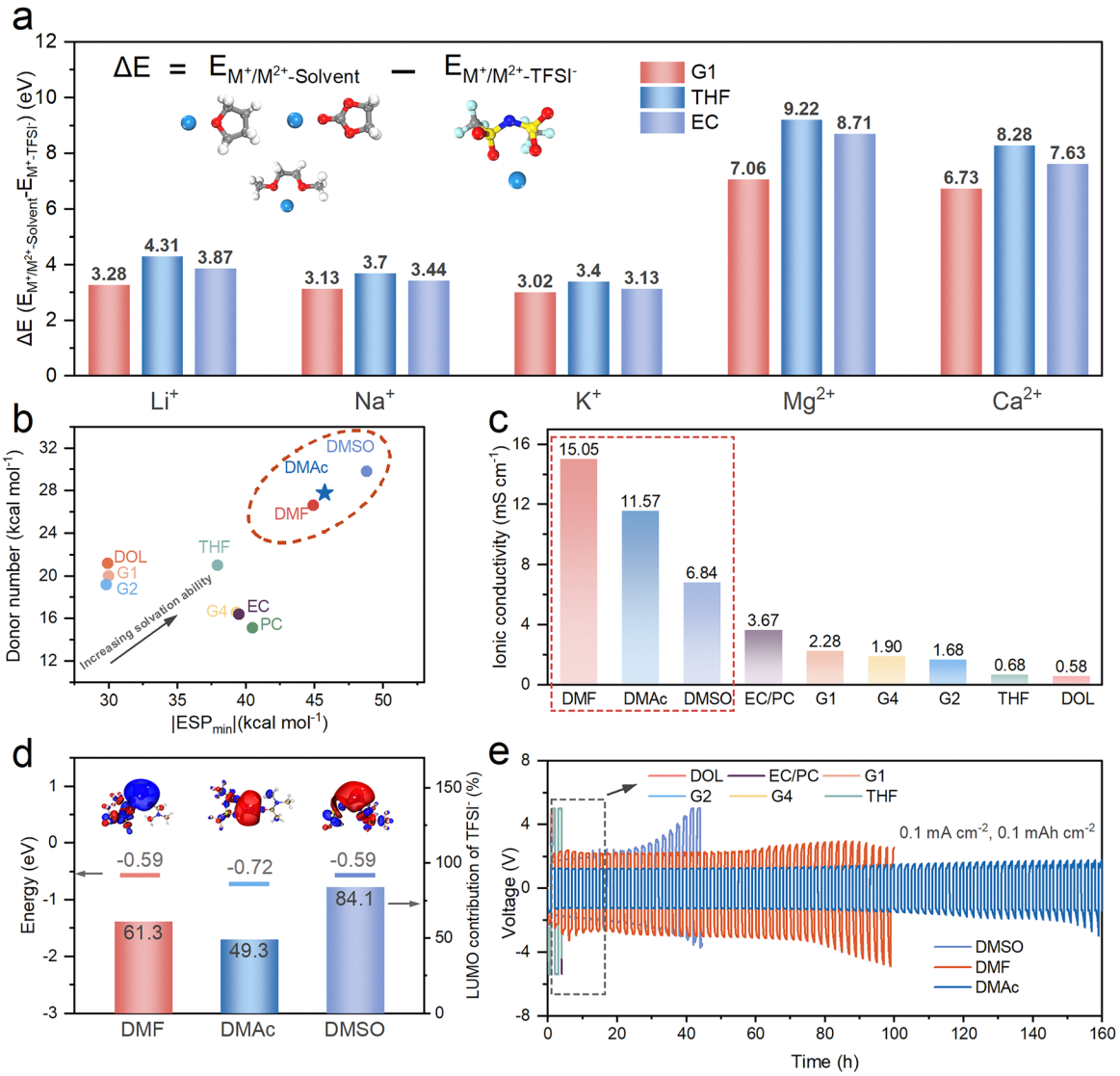

Fig. 2 (a) Binding energy differences between cation–solvent and cation–anion ($\Delta E = E_{M\text{-Solvent}} - E_{M\text{-TFSI}^-}$) in M-TFSI$^-$/solvent electrolytes, M = Li^+, Na^+, K^+, Mg^{2+}, and Ca^{2+} and solvent = G1, THF, and EC. (b) DN *vs.* $|ESP_{min}|$ plots of nine representative solvents. (c) Ionic conductivity of 0.3 M $Ca(TFSI)_2$ in the solvents in (b). (d) LUMO energies and TFSI$^-$ LUMO contribution ratios of three Ca^{2+}–solvent–TFSI$^-$ (solvent = DMF, DMAc, and DMSO) complexes. (e) Cycling performance of Ca//Ca symmetric cells in 0.3 M $Ca(TFSI)_2$ DMAc, DMF, and DMSO electrolytes at 0.1 mA cm^{-2} and 0.1 mAh cm^{-2}.

electrolytes (0.3 M $Ca(TFSI)_2$ in DMF, DMAc, or DMSO) exhibit higher ionic conductivities (σ = 6.84 to 15.05 mS cm^{-1}) than the moderate or weakly solvating systems (σ = 0.58 to 3.67 mS cm^{-1}) under the identical 0.3 M salt concentration (Fig. 2c and Fig. S6). Interestingly, galvanostatic cycling of Ca//Ca symmetric cells in these electrolytes at 0.1 mA cm^{-2} and 0.1 mAh cm^{-2} (Fig. 2e) displays reversibility only in the DMF, DMAc, and DMSO-based electrolytes, whereas the cells employing the G1, G2, G4, THF, DOL and EC/PC-based electrolytes rapidly fail by exceeding the 5 V cutoff voltage.

Among the three workable electrolytes, the cyclability of Ca//Ca cells follows the order of DMAc (160 h) > DMF (100 h) > DMSO (40 h) at 0.1 mA cm^{-2}, despite the calculated binding energies between solvents and Ca^{2+} following a different trend (DMSO > DMAc > DMF, Fig. S7). This discrepancy suggests that, beyond solvation strength, the electrochemical stability of Ca^{2+}–solvent–TFSI$^-$ complexes and the resulting SEI composition play an unignorable role in determining the reversibility of Ca metal anodes. Accordingly, we calculated the LUMO levels of Ca^{2+}–solvent–TFSI$^-$ (solvent = DMF, DMAc, and DMSO) complexes and analyzed the LUMO contributions from TFSI$^-$ (Fig. 2d). Although their overall LUMO levels are comparable (−0.59 to −0.72 eV), corresponding to similar reductive stability, the TFSI$^-$ contributions to the LUMO are largely different, namely, 49.3% for Ca^{2+}–DMAc–TFSI$^-$, 61.3% for Ca^{2+}–DMF–TFSI$^-$, and 84.1% for Ca^{2+}–DMSO–TFSI$^-$. Interestingly, the observed cyclability (DMAc > DMF > DMSO) of Ca electrodes correlated inversely with the TFSI$^-$ contribution to the LUMO. It means that higher TFSI$^-$ stability in the Ca^{2+}–solvent–TFSI$^-$ complex can suppress TFSI$^-$ decomposition into unfavorable inorganic SEI species, thus

stabilizing the electrochemical reduction of Ca metal anodes. Overall, these results establish that strong Ca^{2+} solvating capability and the high stabilization degree of $TFSI^-$ can be considered as the primary criteria for selecting optimal solvents in $Ca(TFSI)_2$-based electrolytes. Having established DMAc as the ideal solvent, we further evaluated the concentration-dependent anion-coupling behavior. The physicochemical properties of electrolytes and resulting electrochemical performance of Ca electrodes recommend 0.3 M $Ca(TFSI)_2$–DMAc as the optimal choice (Fig. S8).

2.2 Anion-pulling halogen benzene additives

Despite the reversibility achieved in $Ca(TFSI)_2$–DMAc electrolytes, the high overpotentials of >1 V for Ca metal plating/stripping reactions remain unsatisfactory. To further ameliorate the reaction kinetics, a series of halogenated benzenes were screened as anion-pulling additives to further decouple the Ca^{2+}–$TFSI^-$ ion pairs. The polarizable aromatic framework and electron-withdrawing halogens confer strong electropositivity for the aromatic C–H bonds (Fig. S9), which favors the formation of C–H···O hydrogen bonds with $TFSI^-$. Fig. S10a presents the C–H···O binding energies of various halogenated benzenes and DMAc with $TFSI^-$, namely, −36.86 kJ mol^{-1} for 1,2-dichlorobenzene (1,2-DCB), −37.28 kJ mol^{-1} for 1,2-DBB, −34.78 kJ mol^{-1} for 1,2-difluorobenzene (1,2-DFB), and −34.96 kJ mol^{-1} for DMAc, respectively. Remarkably, the Ca deposition/stripping overpotential decreases nearly linearly with increasing C–H···O binding energies, reaching a minimum of 0.32 V at 0.2 mA cm^{-2} in the 0.3 M $Ca(TFSI)_2$–DMAc/1,2-DBB electrolyte (Fig. 3a and Fig. S10b). The 1.1 V reduction from $Ca(TFSI)_2$–DMAc to $Ca(TFSI)_2$–DMAc/1,2-DBB suggests the effectiveness of the anion-pulling strategy. It is noted that although 1,2-DFB and DMAc present comparable binding energies with $TFSI^-$, the 1,2-DFB additive significantly increases the overpotential to 3.2 V (from 1.4 V for the baseline DMAc electrolyte), which is likely attributable to the 1,2-DFB-derived fluorinated inorganic species in the SEI layer.

For the interaction between 1,2-DBB additives and Ca^{2+}, DFT calculations exhibit markedly lower $|ESP_{min}|$ values (*i.e.*, 14.79 kcal mol^{-1} for 1,2-DBB *vs.* 45.78 kcal mol^{-1} for DMAc) and binding energies (*i.e.*, −83.83 kcal mol^{-1} for Ca^{2+}-1,2-DBB *vs.* −115.19 kcal mol^{-1} for Ca^{2+}–DMAc) (Fig. S11). It is inferred that the 1,2-DBB additive does not enter the first solvation shell but instead exerts its pulling effect externally on $TFSI^-$. Other bromine benzene additives with different numbers of bromine substituents, like 1-bromobenzene (1-BB) and 1,3,5-tribromobenzene (1,3,5-TBB), were also examined that present lower binding energies with $TFSI^-$ and inferior electrochemical performance for Ca metal anodes (Fig. S12). By cycling Ca//Ca symmetric cells in DMAc/1,2-DBB electrolytes with different 1,2-DBB ratios (0.1 vol%, 0.2 vol%, 0.5 vol%, and 1.0 vol%, Fig. S13), the 0.5 vol% 1,2-DBB was determined as the optimal choice with the best cyclability of Ca metal for the subsequent studies.

Raman and nuclear magnetic resonance (NMR) measurements were carried out to evaluate the solvation perturbation induced by 1,2-DBB. Upon dissolving $Ca(TFSI)_2$ in DMAc, the characteristic Raman peak at 1143.8 cm^{-1} referring to the S=O vibration of $TFSI^-$ downshifts to 1141.5 cm^{-1}, and further to 1140.4 cm^{-1} with 1,2-DBB addition (Fig. 3c), signifying noticeable decoupling of $TFSI^-$ anions. The strong interaction between $TFSI^-$ and 1,2-DBB is further evidenced by the concurrent redshifts in the C–H in-plane and C–C–C out-of-plane bending vibrations of 1,2-DBB Raman spectra (Fig. S14). These spectral changes can be attributed to the redistribution of electron density at the C–H donor site and distortion of the aromatic ring in 1,2-DBB upon binding with $TFSI^-$.[38] Moreover, the downfield shift of ^1H NMR peaks for 1,2-DBB (at both 0.5 vol% and 3 vol% concentrations) further illustrates the electron-withdrawing effect of the C–H sites in 1,2-DBB on $TFSI^-$ (Fig. 3d). Similarly, the downfield shift in the ^{19}F NMR chemical shifts of $TFSI^-$ anions upon adding 1,2-DBB (Fig. S15) also supports the anion-pulling mechanism.[39]

The binding configurations between $TFSI^-$ and DMAc or 1,2-DBB were calculated using DFT. It shows a shorter C–H···O length of 2.40 Å for 1,2-DBB–$TFSI^-$ than that of 2.66 Å for DMAc–$TFSI^-$ (Fig. S16a). Meanwhile, enhanced C–F, S–N and S–O bonding orders in $TFSI^-$ upon bonding with 1,2-DBB suggests greater thermodynamic stability of $TFSI^-$ (Fig. S16b). The strong noncovalent interactions were further visualized *via* interaction region indicator (IRI) isosurfaces (Fig. 3b).[40] MD simulations reveal that 1,2-DBB forms external complexes with $TFSI^-$ without entering the primary Ca^{2+} solvation shell (Fig. 3e). RDFs (Fig. 3f and g) show that the coordination numbers of Ca–O_{TFSI^-} decrease from 2.1 to 1.5, while the Ca–O_{DMAc} increases from 5.7 to 6.3 to preserve solvation stability. Critically, 1,2-DBB was not observed in the primary solvation shell, consistent with their weaker binding energy to Ca^{2+} (Fig. S17). The rearrangement of DMAc coordination was further validated by spectroscopic evidence: the downshifts of the ^{13}C NMR chemical shift (Fig. 3h and Fig. S18) in the DMAc solvent following the 1,2-DBB addition indicated enhanced Ca^{2+}–DMAc interaction. This enhancement is corroborated by Raman spectra, which reveal an increased percentage of coordinated DMAc molecules from 42.7% to 49.2% (Fig. S19). The effective anion-decoupling resulted in an increased ionic conductivity from 11.57 to 12.75 mS cm^{-2} (Fig. S20), confirming the accelerated Ca^{2+} transport in the DMAc/1,2-DBB electrolyte.

Building on the MD-derived coordination number (7.8), a representative Ca^{2+} solvation structure comprising five DMAc and one $TFSI^-$ anion was modeled. In the presence of 1,2-DBB, DFT results show elongated and weakened Ca^{2+}–$TFSI^-$ bonds arising from the extraction of $TFSI^-$ from the solvation shell by 1,2-DBB. Conversely, the Ca^{2+}–DMAc coordination presents shorter bond lengths and higher bond orders to compensate for the Ca^{2+} polarization left by $TFSI^-$ deficiency (Fig. S21). Moreover, the presence of 1,2-DBB reduces the desolvation free energy of Ca^{2+}, reaching a minimum upon complete $TFSI^-$ removal, indicating that anion decoupling accelerates desolvation kinetics (Fig. 2i). Temperature-dependent electrochemical impedance spectroscopy (EIS) analyses (Fig. 2j and Fig. S22) also reveal lower Ca^{2+} desolvation energies in the DMAc/1,2-DBB electrolyte (ΔE = 27.02 kJ mol^{-1}) compared with pristine

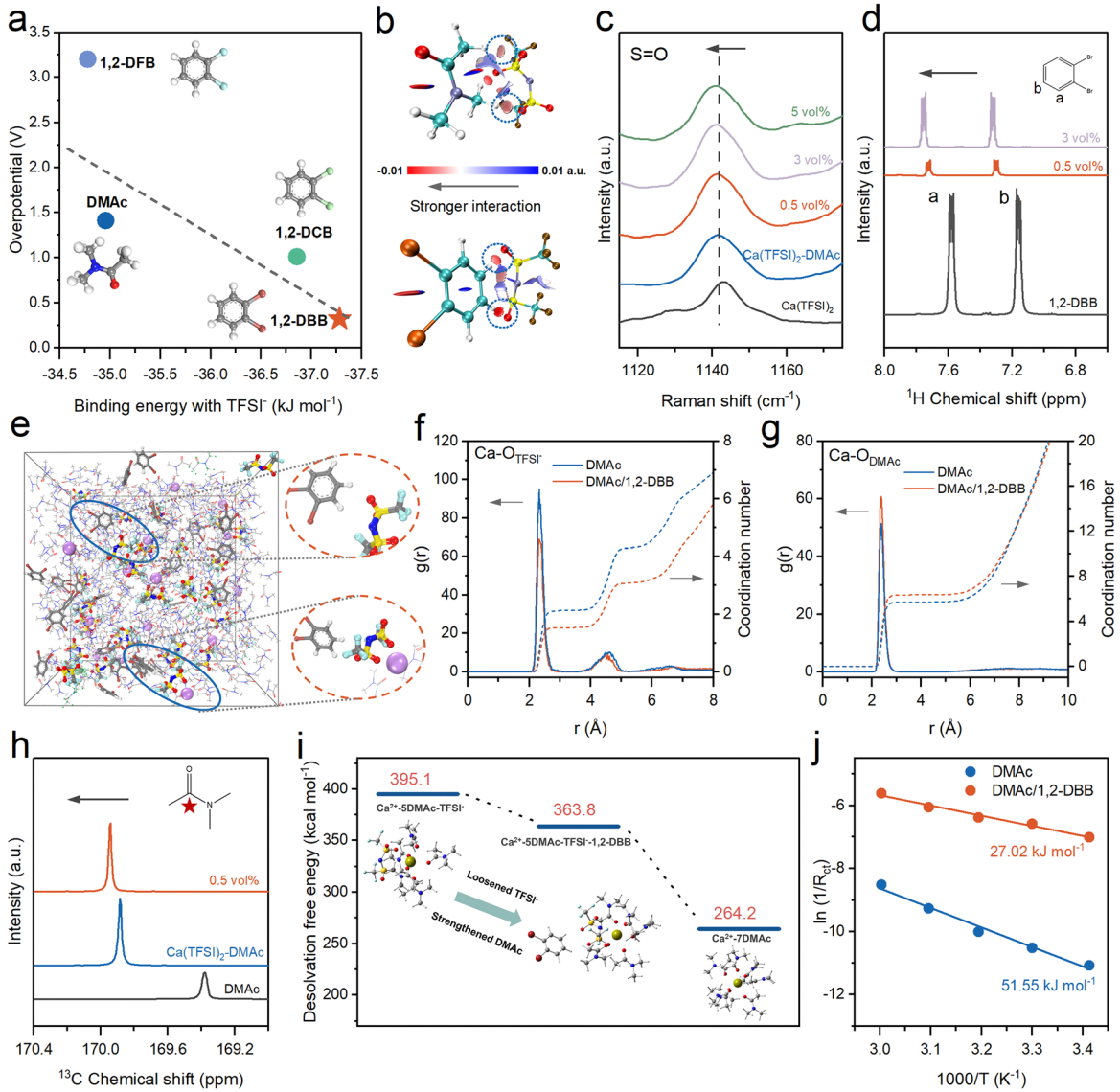

Fig. 3 (a) Correlation between the binding energies of DMAc, 1,2-DFB, 1,2-DCB and 1,2-DBB with $TFSI^-$ and the overpotentials of Ca//Ca symmetric cells cycling in corresponding electrolytes. (b) IRI isosurfaces image of noncovalent interactions between $TFSI^-$ and DMAc (bottom) or 1,2-DBB (top). (c) Raman spectra of the $Ca(TFSI)_2$ salt, DMAc electrolyte, and DMAc/1,2-DBB electrolytes. (d) ^1H NMR spectra of pure 1,2-DBB and DMAc/1,2-DBB electrolytes with 0.5 vol% and 3 vol% 1,2-DBB. (e) The snapshot from the MD simulation box of the DMAc/1,2-DBB electrolyte. RDFs (solid lines) and coordination number (dashed lines) for (f) $Ca-O_{TFSI}$ and (g) $Ca-O_{DMAc}$ in different electrolytes. (h) ^{13}C NMR spectra of DMAc solvent, DMAc electrolyte, and DMAc/1,2-DBB electrolyte. (i) DFT calculated Ca^{2+} desolvation energies of different solvation structures. (j) Arrhenius plots to calculate the Ca^{2+} desolvation energies in the DMAc and DMAc/1,2-DBB electrolytes.

DMAc (ΔE = 51.55 kJ mol^{-1}), consistent with the faster interfacial kinetics. In addition, the $TFSI^-$ contribution to the LUMO decreases from 11.1% to 3.4% upon 1,2-DBB addition (Fig. S23), suggesting improved reductive stability of $TFSI^-$ and regulated SEI chemistry to be discussed below.

2.3 Solid electrolyte interphases from anion-decoupled electrolytes

The anion-decoupling strategy not only facilitates ion transport in the bulk electrolyte and the Ca^{2+} desolvation kinetics at the electrolyte/electrode interface but also importantly influences the SEI composition and Ca stripping/plating behaviors. After 20 cycles in Ca//Ca symmetric cells in the DMAc electrolyte, the cycled Ca anodes were covered by a fluorine (F)-rich passivation layer (Fig. 4a) in comparison to pristine Ca foil (Fig. S24a and b). XRD analysis identifies crystalline $Ca(OH)_2$, CaO, and CaF_2 as the dominant inorganic species on the Ca metal surface (Fig. 4c). In contrast, Ca metal electrodes cycled in the DMAc/1,2-DBB electrolyte present a uniform surface with significantly reduced F content (Fig. 4b and Fig. S24c), consistent with the negligible CaF_2 peaks in the XRD result. HRTEM was employed to examine the microstructure and composition of the SEI. Ca metal anodes cycled in the DMAc electrolyte present a thick SEI layer (~23.5 nm) containing CaF_2

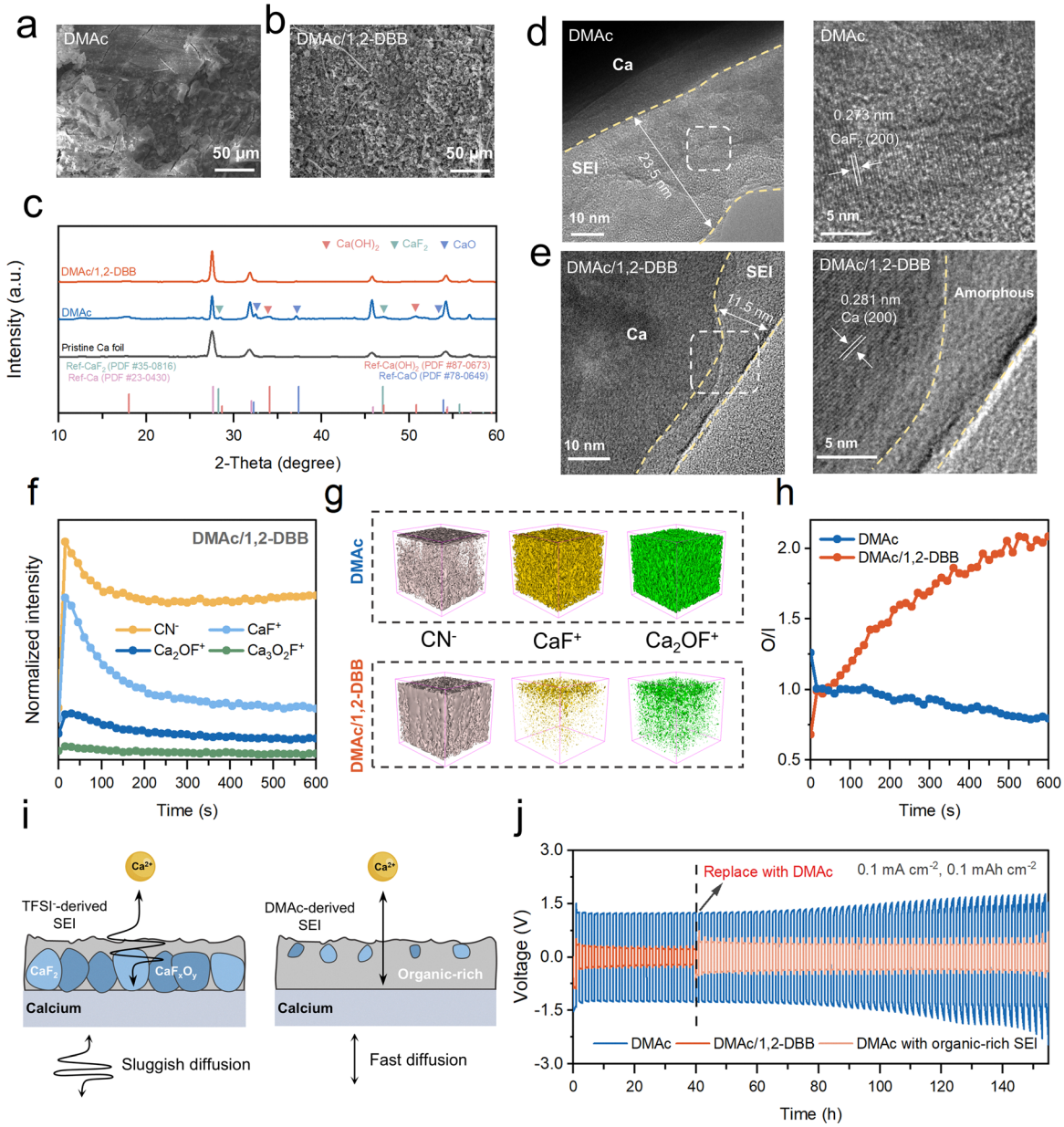

Fig. 4 SEM images of cycled Ca metal anodes in the (a) DMAc and (b) DMAc/1,2-DBB electrolytes. (c) XRD patterns of the pristine Ca foil, Ca metal anodes cycled in DMAc, and DMAc/1,2-DBB electrolytes. HRTEM images of SEI layers formed in the (d) DMAc and (e) DMAc/1,2-DBB electrolytes. (f) TOF-SIMS depth profiles of Ca anodes after cycling in the DMAc/1,2-DBB electrolyte. (g) TOF-SIMS 3D reconstruction of CN^-, CaF^+ and Ca_2OF^+ in the SEI formed in DMAc electrolyte (up) and DMAc/1,2-DBB electrolyte (bottom). (h) The depth profile of the organic to inorganic component ratios (O/I) in the SEI formed in these two electrolytes. (i) Schematic illustration of Ca^{2+} transport across the inorganic-rich SEI (left) and organic-rich SEI (right) formed in DMAc and DMAc/1,2-DBB electrolytes, respectively. (j) Voltage profiles of Ca//Ca symmetric cells cycling in DMAc, DMAc/1,2-DBB (before 40th hour) + DMAc (after 40th hour) electrolytes.

nanocrystals with a lattice fringe of 0.273 nm (Fig. 4d). The SEI formed in the DMAc/1,2-DBB electrolyte is thinner (~11.5 nm) and shows an amorphous organic layer on the surface of metallic Ca deposits (Fig. 4e). Furthermore, characterization of SEI layers formed in the DMAc/1,2-DCB and DMAc/1,2-DFB electrolytes reveals a clear correlation between the anion-decoupling ability of the additives and the resulting SEI properties (Fig. S25).

The chemical composition and depth distribution of SEI layers were further elucidated by X-ray photoelectron spectroscopy (XPS) depth profiling and time-of-flight secondary ion mass spectrometry (TOF-SIMS). After cycling in the DMAc electrolyte, the F 1s spectrum shows a high content of Ca–F species (Fig. S26a), which become more prominent with increasing Ar^+ etching time. This result indicates abundant CaF_2 throughout the SEI layer on the Ca metal surface, a consequence of aggressive $TFSI^-$ decomposition. Conversely, in the DMAc/1,2-DBB electrolyte, the normalized F 1s peak intensities for inorganic species are much lower (Fig. S26b) along with increased C–F_x peaks (Fig. S27). Such a difference

confirms the suppressed $TFSI^-$ decomposition and stabilization of C–F bonds by the 1,2-DBB additive. Similar trends are also observed in the S 2p and N 1s spectra (Fig. S28 and S29).

XPS depth profiling revealed a hierarchical SEI structure in the DMAc electrolyte, where the inorganic components (*i.e.*, CaF_2 and CaS_x) from $TFSI^-$ decomposition become increasingly prominent upon etching, while organic components diminished rapidly with depth (Fig. S27). Conversely, the SEI from the DMAc/1,2-DBB electrolyte exhibited a reduced inorganic content and abundant organic components upon etching, indicating the formation of a solvent-derived, organic-rich SEI promoted by the anion-pulling effect. These SEI characteristics were further corroborated by TOF-SIMS. The SEI formed in the DMAc/1,2-DBB electrolyte was dominated by solvent-derived organic species (CN^- and C_2^-), alongside minor inorganic fluorides (Fig. 4f–h and Fig. S30). In contrast, the SEI derived from the DMAc electrolyte shows a high prevalence of CaF^+, Ca_2OF^+, and $Ca_3O_2F^+$ throughout the depth, while organic components are rich only on the top surface (Fig. 4g and Fig. S31a–c). Sulfur-containing species (S^-, SO^-, and SO_2^-),

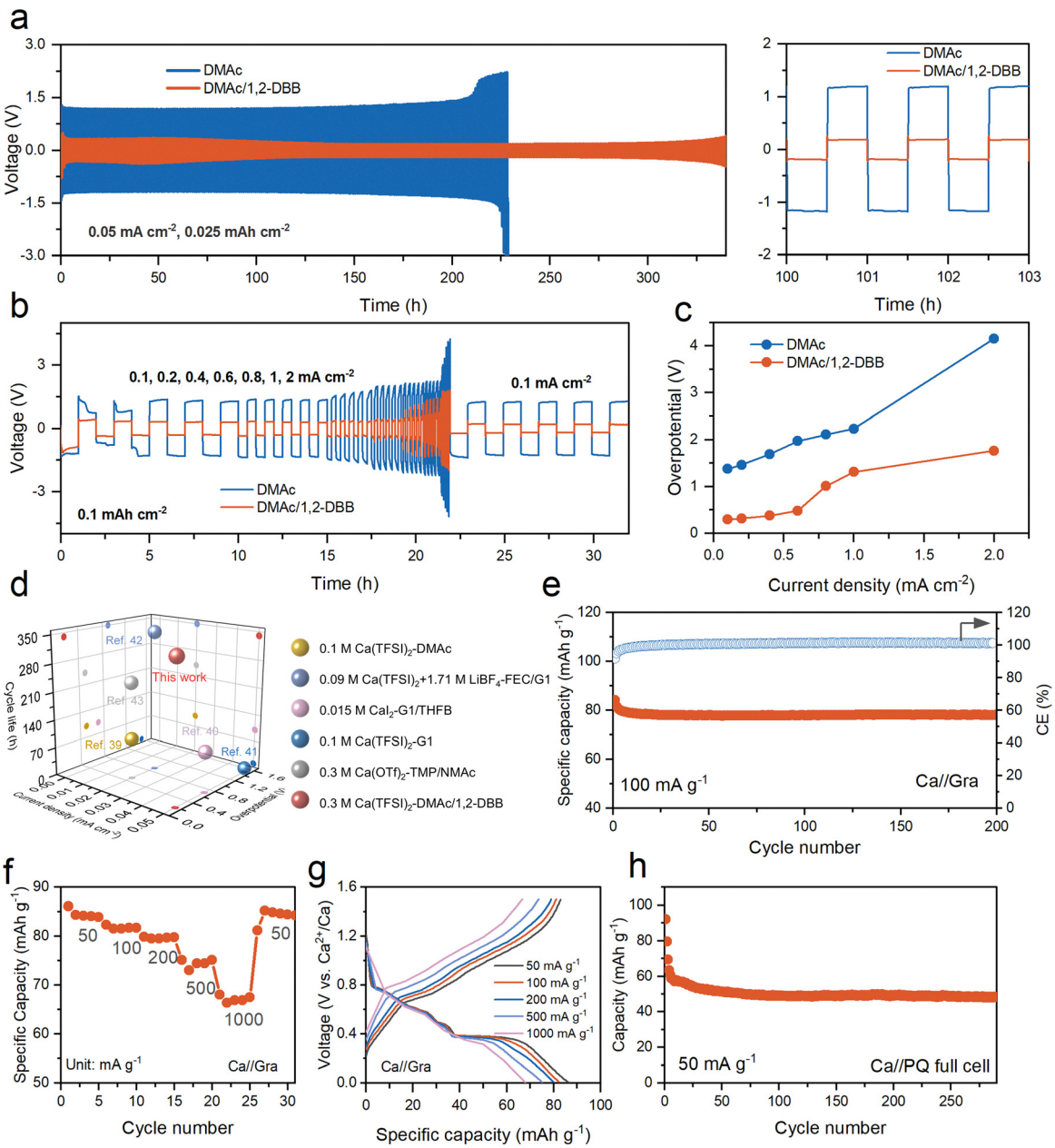

Fig. 5 (a) Cycling performance of Ca//Ca symmetric cells in DMAc and DMAc/1,2-DBB electrolytes at 0.05 mA cm^{-2} and 0.025 mAh cm^{-2}. (b) Rate performance of Ca//Ca symmetric cells in DMAc and DMAc/1,2-DBB electrolytes at a constant capacity of 0.1 mAh cm^{-2}. (c) Overpotentials of Ca//Ca cells at increasing current rates derived from (b). (d) Comparison of the electrochemical performance of Ca//Ca symmetric cells in recently reported electrolytes.[40–44] (e) Cycling performance, (f) rate performance and (g) charge–discharge curves of the Ca//Gra cell in the DMAc/1,2-DBB electrolyte. (h) Cycling performance of the Ca//PQ full cell in the DMAc/1,2-DBB electrolyte.

which are solely derived from $TFSI^-$ anions, are also greatly reduced upon 1,2-DBB addition (Fig. S31d). Quantitative analysis of the organic-to-inorganic component (O/I) ratios from TOF-SIMS depth profiles (Fig. 4h) highlights this contrast: the internal SEI formed in the DMAc/1,2-DBB electrolyte reached an O/I value of 2.1, compared to 0.8 for the SEI in the DMAc electrolyte demonstrates the suppression of $TFSI^-$ decomposition. To confirm the superiority of the organic-rich SEI, an electrolyte replacement protocol was implemented (Fig. 4i and j). When cycled directly in the DMAc electrolyte, the $TFSI^-$-derived SEI with sluggish Ca^{2+} diffusion feature results in a high overpotential of 1.27 V. In contrast, Ca metal electrodes pre-cycled in the DMAc/1,2-DBB electrolyte and subsequently transferred to the DMAc electrolyte exhibited a much lower overpotential of 0.55 V, indicating the persistent benefit of the pre-formed organic-rich SEI.

To evaluate the possible reduction of the 1,2-DBB additive on Ca metal, Ca electrodes were immersed in pure 1,2-DBB for 24 h before assembling symmetric cells with DMAc electrolyte. The resulting voltage profiles remain unchanged relative to the untreated Ca//Ca cells (Fig. S32). Furthermore, *in situ* Raman spectroscopy monitored the electrolyte evolution during cycling (Fig. S33). The 1,2-DBB signal at 399.1 cm^{-1} remained constant in both the intensity and the peak position, whereas the characteristic DMAc peak at 589.7 cm^{-1} presents apparent attenuation during the initial cycles before approaching stabilization. Consistently, no bromine-containing species were detected in the TOF-SIMS spectrum for the SEI (Fig. S34). These results collectively demonstrate that 1,2-DBB acts solely as an anion-pulling modulator without direct participation in interfacial reactions, which differs from the reported role of 1,2-DBB decomposition in forming a NaBr-rich SEI in Na metal batteries.[41]

2.4 Electrochemical performance of Ca metal anodes

To validate the efficacy of the anion-decoupled electrolyte, electrochemical performance of Ca metal anodes was systematically evaluated. As shown in Fig. 5a, the Ca//Ca symmetric cell in the DMAc/1,2-DBB electrolyte achieves an extended cycling lifetime of 340 h at 0.05 mA cm^{-2} and 0.025 mAh cm^{-2}. In comparison with a high overpotential of 1.68 V in the DMAc electrolyte, the overpotential reduced by nearly nine-fold to 0.19 V. Even under a ten-fold higher current density of 0.5 mA cm^{-2}, the cells with DMAc/1,2-DBB electrolyte persisted stability over 65 cycles (Fig. S35). Furthermore, the DMAc/1,2-DBB electrolyte enabled superior rate capability (Fig. 5b), reducing the overpotentials by two to five times compared to the DMAc electrolyte across current densities ranging from 0.1 to 2 mA cm^{-2} (Fig. 5c). Consistently, the cyclic voltammetry (CV) profiles exhibited pronounced stripping and plating peak currents (Fig. S36), indicative of enhanced reaction kinetics. Benchmarking against state-of-the-art Ca anode performance in various electrolytes highlights that the present anion-decoupled formulation achieves one of the best combinations of low overpotentials, high current responses, and extended cycling stability (Fig. 5d and Table S1).[34,42–45]

Electrochemical impedance spectroscopy (EIS) was employed to probe the interfacial kinetics and their evolution during cycling (Fig. S37). For fresh cells, the charge transfer resistance (R_{CT}) of Ca//Ca symmetric cells in the DMAc/1,2-DBB electrolyte is more than twenty times lower than that in the DMAc electrolyte (Fig. S37a and b). Although impedances increased upon cycling for both systems, the cell with the DMAc/1,2-DBB electrolyte maintained exceptional interfacial stability, with both R_{CT} and SEI resistance (R_{SEI}) reduced by over seven times compared to those in the DMAc electrolyte after 20 cycles (Fig. S37c and d), consistent with the low overpotential and superior rate performance.

CV curves of Ca//carbon paper (CC) asymmetric cells (Fig. S38) exhibited reduced voltage hysteresis and larger current response in the DMAc/1,2-DBB electrolyte than those in the DMAc electrolyte. SEM images and corresponding EDS mapping demonstrated uniform Ca deposits on the CC current collector (Fig. S39). To further verify the kinetic advantage in the DMAc/1,2-DBB electrolyte, we then paired Ca metal with graphite (Gra) electrodes undergoing a rapid co-intercalation reaction in the DMAc-based electrolyte.[46,47] In the DMAc system, Ca//Gra cells suffered severe polarization and negligible capacities due to the high overpotential and poor reversibility of Ca metal anodes (Fig. S40). In contrast, the DMAc/1,2-DBB electrolyte enabled highly reversible discharge/charge over 200 cycles at 100 mA g^{-1} with a stable capacity of 78 mAh g^{-1} (Fig. 5e). When the current density increased by 20-fold from 50 mA g^{-1} to 1000 mA g^{-1}, 79% of the initial capacity was preserved (Fig. 5f) with a distinct discharge plateau at 0.37 V throughout the high-rate cycling (Fig. 5g). The remarkable high-rate capability can be attributed to the appealing reaction kinetics of the Ca metal electrode. The Ca//9,10-phenanthrenequinone (PQ) full cell was also built to deliver decent cyclic capacities exceeding 90 mAh g^{-1} and stable cycling for over 290 cycles (Fig. 5h and Fig. S41), supporting the practical applicability of the tailored electrolyte in Ca-based energy storage, whereas it fails to deliver appreciable capacity in the DMAc electrolyte due to the severe kinetic limitation of the Ca anode (Fig. S42). When extended to other fluorinated Ca salts (*i.e.*, $Ca(BF_4)_2$ and $Ca(OTf)_2$), the addition of 1,2-DBB can also significantly reduce the Ca plating/stripping overpotentials, which suggests the broad applicability of our anion-decoupling strategy across diverse Ca electrolytes (Fig. S43). Finally, we also prove the effectiveness of our anion-decoupling strategy for Mg metal anodes by cycling Mg//Mg cells in $Mg(TFSI)_2$-G1, DMAc, and DMAc/1,2-DBB electrolytes, where similar reductions in the plating/stripping overpotentials are observed (Fig. S44), implying the general applicability of this electrolyte design principle for multivalent metal anodes.

3. Conclusions

In summary, we revealed the critical role of anion-decoupling chemistry in enhancing the reaction kinetics and cycling stability of Ca metal anodes in $Ca(TFSI)_2$-based electrolytes. By integrating a strongly coordinating DMAc solvent with the anion-pulling 1,2-DBB additive, the Ca^{2+}–$TFSI^-$ coupling is significantly weakened, rendering the strength of Ca^{2+}–solvent

coordination, high ionic conductivity (12.75 mS cm^{-1}), and reduced desolvation energy barriers at the electrode/electrolyte interface. More importantly, this decoupling strategy improves the stability of $TFSI^-$ and suppresses its decomposition into undesirable inorganic compounds. The organic-rich SEI from a solvent-rich electrolyte configuration facilitates Ca^{2+} transport and electrodeposition with low overpotentials. Effectiveness of the anion-decoupled electrolyte is demonstrated by the stable cycling of Ca//Ca symmetric cells in the $Ca(TFSI)_2$–DMAc/1,2-DBB electrolyte, in comparison to the high overpotentials of >5 V and short cycle life of Ca metal electrodes in conventional electrolytes. The anion-decoupled DMAc/1,2-DBB electrolyte also sustains Ca//Gra and Ca//PQ full cells over 200 cycles with $>90\%$ capacity retention. These findings highlight a unique electrolyte design paradigm, fundamentally distinct from monovalent metal anodes which prefer strong anion coordination in the electrolyte systems, offering new insights for advancing sustainable and safe multivalent metal anodes.

Author contributions

Conceptualization, methodology and formal analysis: Q. Meng and Z.-L. Xu; data curation, investigation, project administration, visualization and writing – original draft: Q. Meng; resources and validation: Z. Zhan; funding acquisition and resources: Z.-L. Xu, Y. Y. Ma, Q. Qi, Y. K. Hua, Y. Y. Yi, J. Y. Yu, and M. C. Wu; supervision: Z.-L. Xu; writing – reviewing and editing: J. J. Tang, S. H. Cai, K. C. Chan and Z.-L. Xu.

Conflicts of interest

There are no conflicts to declare.

Data availability

The data supporting this article have been included as part of the supplementary information (SI). Supplementary information is available. See DOI: https://doi.org/10.1039/d5ee07317k.

Acknowledgements

This work described in this paper was fully supported by grants from the Research Grants Council of the Hong Kong Special Administrative Region, China (Project No. PolyU15305022 and PolyU15304723), the Research Institute for Advanced Manufacturing (Project No. 1-CDLR), the Research Committee of the Hong Kong Polytechnic University (Project No. G-UARH, 1-BBR0, and 4-W43C), the General Program Sponsored by Basic Research Fund in Shenzhen Natural Science Foundation (Project No. JCYJ20250604184257074), and the NSFC/RGC Joint Research Scheme (Project No. N_PolyU5117/25).

References

1 J. Kim, M. Kim, J. Lee, J. An, S. Yang, H. C. Ahn, D.-J. Yoo and J. W. Choi, *Chem. Soc. Rev.*, 2024, **53**, 8878–8902.
2 Y. Liang, H. Dong, D. Aurbach and Y. Yao, *Nat. Energy*, 2020, **5**, 646–656.
3 H. Lin, J. Yu, F. Chen, R. Li, B. Y. Xia and Z. L. Xu, *Small Methods*, 2023, **7**, 2300561.
4 I. D. Hosein, *ACS Energy Lett.*, 2021, **6**, 1560–1565.
5 Y. Hua, Y. Ma, Q. Qi and Z.-L. Xu, *Nanoscale*, 2024, **16**, 17683–17698.
6 R. Li, Y. Lee, Z. Song, S. Ma, Y. Yi, H. Lin, Y. Hua, P. Jiang, F. Chen, J. Yu, X. Pu, Z. Chen, K. C. Chan, K.-Y. Park and Z.-L. Xu, *Adv. Mater.*, 2025, **37**, e06603.
7 H. Lin, Q. Meng, J. Long, C. Cao, and Z. L. Xu, *Adv. Funct. Mater.*, 2026, e00035.
8 S. Li, J. Zhang, S. Zhang, Q. Liu, H. Cheng, L. Fan, W. Zhang, X. Wang, Q. Wu and Y. Lu, *Nat. Energy*, 2024, **9**, 285–297.
9 M. E. Arroyo-de Dompablo, A. Ponrouch, P. Johansson and M. R. Palacín, *Chem. Rev.*, 2019, **120**, 6331–6357.
10 J. Forero-Saboya, C. Davoisne, R. Dedryvère, I. Yousef, P. Canepa and A. Ponrouch, *Energy Environ. Sci.*, 2020, **13**, 3423–3431.
11 D. Aurbach, R. Skaletsky and Y. Gofer, *J. Electrochem. Soc.*, 1991, **138**, 3536.
12 S. Yang, X. Wang, R. Li, Y. Zhou, H. Huang, M. Zhou, Y. Gao, W. Zhao, Y. Gao and Z. Pan, *Energy Environ. Sci.*, 2025, **18**, 1941–1951.
13 A. M. Melemed and B. M. Gallant, *J. Electrochem. Soc.*, 2020, **167**, 140543.
14 B. Ji, H. He, W. Yao and Y. Tang, *Adv. Mater.*, 2021, **33**, 2005501.
15 H. Wan, J. Xu and C. Wang, *Nat. Rev. Chem.*, 2024, **8**, 30–44.
16 X. Liu, X. Dong, H. Adenusi, Y. Wu and S. Passerini, *Nat. Rev. Chem.*, 2025, 1–12.
17 H. Lin, Z. Zhan, H. Zeng, R. Li, Y. Yi, F. Chen, S. Cai, Y. Zhu, C. F. Cheung and Z.-L. Xu, *Adv. Mater.*, 2025, e10711.
18 A. Ponrouch, C. Frontera, F. Barde and M. R. Palacin, *Nat. Mater.*, 2016, **15**, 169–172.
19 D. Wang, X. Gao, Y. Chen, L. Jin, C. Kuss and P. G. Bruce, *Nat. Mater.*, 2018, **17**, 16–20.
20 Z. Li, O. Fuhr, M. Fichtner and Z. Zhao-Karger, *Energy Environ. Sci.*, 2019, **12**, 3496–3501.
21 A. Shyamsunder, L. E. Blanc, A. Assoud and L. F. Nazar, *ACS Energy Lett.*, 2019, **4**, 2271–2276.
22 K. Kisu, S. Kim, T. Shinohara, K. Zhao, A. Zuttel and S. I. Orimo, *Sci. Rep.*, 2021, **11**, 7563.
23 T. Pavcnik, J. D. Forero-Saboya, A. Ponrouch, A. Robba, R. Dominko and J. Bitenc, *J. Mater. Chem. A*, 2023, **11**, 14738–14747.
24 Y. Zhao, T. Zhou, M. Mensi, J. W. Choi and A. Coskun, *Nat. Commun.*, 2023, **14**, 299.
25 S. Wang, X.-G. Zhang, Y. Gu, S. Tang and Y. Fu, *J. Am. Chem. Soc.*, 2024, **146**, 3854–3860.
26 S. Ilic, S. N. Lavan and J. G. Connell, *Chem*, 2024, **10**, 2987–3007.

27 J. Tan, J. Matz, P. Dong, J. Shen and M. Ye, *Adv. Energy Mater.*, 2021, **11**, 2100046.
28 H. Yildirim, A. Kinaci, M. K. Y. Chan and J. P. Greeley, *ACS Appl. Mater. Interfaces*, 2015, **7**, 18985–18996.
29 J. D. Forero-Saboya, E. Marchante, R. B. Araujo, D. Monti, P. Johansson and A. Ponrouch, *J. Phys. Chem. C*, 2019, **123**, 29524–29532.
30 R. B. Araujo, V. Thangavel and P. Johansson, *Energy Storage Mater.*, 2021, **39**, 89–95.
31 Z. Hou, R. Zhou, Z. Min, Z. Lu and B. Zhang, *ACS Energy Lett.*, 2023, **8**, 274–279.
32 S. Hou, X. Ji, K. Gaskell, P.-F. Wang, L. Wang, J. Xu, R. Sun, O. Borodin and C. Wang, *Science*, 2021, **374**, 172–178.
33 L. Ye, M. Liao, K. Zhang, M. Zheng, Y. Jiang, X. Cheng, C. Wang, Q. Xu, C. Tang, P. Li, Y. Wen, Y. Xu, X. Sun, P. Chen, H. Sun, Y. Gao, Y. Zhang, B. Wang, J. Lu, H. Zhou, Y. Wang, Y. Xia, X. Xu and H. Peng, *Nature*, 2024, **626**, 313–318.
34 Z. Hou, R. Zhou, Y. Yao, Z. Min, Z. Lu, Y. Zhu, J. M. Tarascon and B. Zhang, *Angew. Chem., Int. Ed.*, 2022, **61**, e202214796.
35 I. Mayer, *J. Comput. Chem.*, 2007, **28**, 204–221.
36 P. Zhou, Y. Xiang and K. Liu, *Energy Environ. Sci.*, 2024, **17**, 8057–8077.
37 Y. Wu, Q. Hu, H. Liang, A. Wang, H. Xu, L. Wang and X. He, *Adv. Energy Mater.*, 2023, **13**, 2300259.
38 G. Shakila, S. Periandy and S. Ramalingam, *Spectrochim. Acta, Part A*, 2012, **86**, 449–455.
39 Z. Zhao, B. Nian, Y. Lei, L. Zhao, M. N. Hedhili, D. Guo, Z. Shi, W. Zhao, J. K. El-Demellawi and Y. Wang, *Adv. Mater.*, 2024, **36**, 2402626.
40 T. Lu and Q. Chen, *Chem.: Methods*, 2021, **1**, 231–239.
41 L. Wang, N. Ren, Y. Yao, H. Yang, W. Jiang, Z. He, Y. Jiang, S. Jiao, L. Song, X. Wu, Z.-S. Wu and Y. Yu, *Angew. Chem., Int. Ed.*, 2023, **135**, e202214372.
42 Z. Hou, R. Zhou, K. Liu, J. Zhu and B. Zhang, *Angew. Chem., Int. Ed.*, 2025, **64**, e202413416.
43 H. Lin, J. Meng, W. Guo, R. Li, Y. Yi, Y. Ma, C. F. Cheung, D. Aurbach and Z.-L. Xu, *Energy Environ. Sci.*, 2024, **17**, 6548–6558.
44 S. Yang, X. Wang, R. Li, Y. Zhou, H. Huang, M. Zhou, Y. Gao, W. Zhao, Y. Gao, Z. Pan and X. Yang, *Energy Environ. Sci.*, 2025, **18**, 1941–1951.
45 Z. Slim, C. Cruz-Cardona, C. Pechberty, T. Hosaka, Z. Mandić, V. Panic and P. Johansson, *ACS Mater. Lett.*, 2025, **7**, 3235–3242.
46 Y. Yi, Y. Xing, H. Wang, Z. Zeng, Z. Sun, R. Li, H. Lin, Y. Ma, X. Pu, M. M. Li, K. Y. Park and Z. L. Xu, *Angew. Chem., Int. Ed.*, 2024, **63**, e202317177.
47 J. Park, Z.-L. Xu, G. Yoon, S. K. Park, J. Wang, H. Hyun, H. Park, J. Lim, Y.-J. Ko, Y. S. Yun and K. Kang, *Adv. Mater.*, 2020, **32**, 1904411.